Surfaces and Interfaces 32 (2022) 102123

Contents lists available at ScienceDirect

Surfaces and Interfaces

journal homepage: www.sciencedirect.com/journal/surfaces-and-interfaces

Photocatalytic activity of defective black-titanium oxide photocatalysts towards pesticide degradation under UV/VIS irradiation

Luminita Andronic [a,*], Martynas Lelis [b], Alexandru Enesca [a], Smagul Karazhanov [c]

[a] Product Design, Mechatronics and Environment Department, Transilvania University of Brasov, Eroilor 29, Brasov 500036, Romania
[b] Centre for Hydrogen Energy Technologies, Lithuanian Energy Institute, Breslaujos st. 3, Kaunas LT-44403, Lithuania
[c] Solar Energy Department, Institute for Energy Technology, PO Box 40, Kjeller NO-2027, Norway

ARTICLE INFO

Keywords:
Visible-light photocatalyst
Titanium oxide
Defect centres
Heterogeneous photocatalysis
Pesticides

ABSTRACT

Wastewater treatment containing pesticides has become an intensively studied field in recent years. Titanium dioxide is the most efficient photocatalyst that uses UV radiation, but the photocatalytic properties can be improved under visible radiation conditions. The photocatalytic properties of titanium oxide are closely related to materials defect disorders, such as oxygen vacancy and Ti^{3+} defect. Therefore, defective TiO_2 or black TiO_2 nanoparticles are attractive materials for heterogeneous photocatalysis. Defective nanoparticles with superior properties to white TiO_2 and efficient solar harvest in the photocatalytic application were synthesised in two convenient and low-cost steps via facile sol-gel and $NaBH_4$ reduction techniques. In the reduction step of the white titanium dioxide powder, the defects were controlled by varying the TiO_2: $NaBH_4$wt ratio at 350 °C for 1 h in an argon atmosphere, obtaining powders with shades of grey to black. The characterisation measurements include structure (XRD, XPS, EDS), morphology (SEM), optical properties (UV–vis DRS spectra), and particles (surface area, porosity, DLS particle size distribution) were applied to investigate the properties of nano-structured defective TiO_2. EDS analysis revealed that the O: Ti ratio for the white TiO_2 powder sample was approximately 1.7, which decreased from 1.7 to 1.6 and 1.4 as the TiO_2:$NaBH_4$ ratio was 4:1, 2:1 and 1:1, respectively. Photocatalytic activity of black titanium oxide under visible light was over 90% of imidacloprid degradation and can be associated with the specific surface area, bandgap energy smaller than white TiO_2, a large amount of surface defect Ti^{3+} and oxygen vacancies that promote charge carriers' separation.

1. Introduction

The release of neonicotinoid pesticides is a significant concern for the environment due to their high mobility in the soil and the contamination of groundwater and surface water [1]. For example, imidacloprid is one of the most widely used neonicotinoid pesticides, effective against agricultural pests, so it appears in the aquatic environment in increasing concentrations, affecting insects, birds, crustaceans, fish, and organisms in the soil by increasing acidity [2,3].

Advanced oxidation processes (AOP) are degradation processes of organic pollutants, in particular pesticides, based on reactive oxygen species (ROS) generated on the photocatalyst surface. Titanium oxide-based heterogeneous photocatalysis for pollutant degradation has been investigated over decades [4] and is based on the reaction between a broad range of organic pollutants and ROS species [5]. The generally accepted steps in heterogeneous photocatalytic processes [6–10] are exemplified by considering the most common photocatalyst, titanium dioxide. A photocatalyst is activated by a radiation having $h\nu > E_g$ (E_g = bandgap energy), when electrons (e^-) and holes (h^+) are generated Eq. (1)) in the conduction and valence band, respectively, [11]. Holes participate in oxidation processes, such as organic compounds (Red_1) (Eq. (3)), H_2O (Eq. (4)) or hydroxyl ions (HO^-) (Eq. (5)), and electrons participate in reduction processes (Eqs. (6) and ((9)), if which they do not combine each other Eq. (2)) [12]. ROS species are generated in the photocatalysis process, so electrons and holes in Eq. (1), hydroxyl radicals ($HO^{\cdot}$) in Eqs. (4) and ((5), and superoxide radicals ($O_2^{-\bullet}$) in Eq. (6). Superoxide radicals fulfil the role of oxidising agents in reacting with species formed on the catalyst's surface. Superoxide radicals react with protons to form $HO_2^{\bullet}$ radicals (Eq. (7)), then superoxide radicals form O_2 and H_2O_2 molecules (Eq. (8)). Finally, the electrons in the CB react with the oxidant species according to Eq. (9).

* Corresponding author.
E-mail address: andronic-luminita@unitbv.ro (L. Andronic).

https://doi.org/10.1016/j.surfin.2022.102123
Received 13 April 2022; Received in revised form 24 May 2022; Accepted 9 June 2022
Available online 16 June 2022

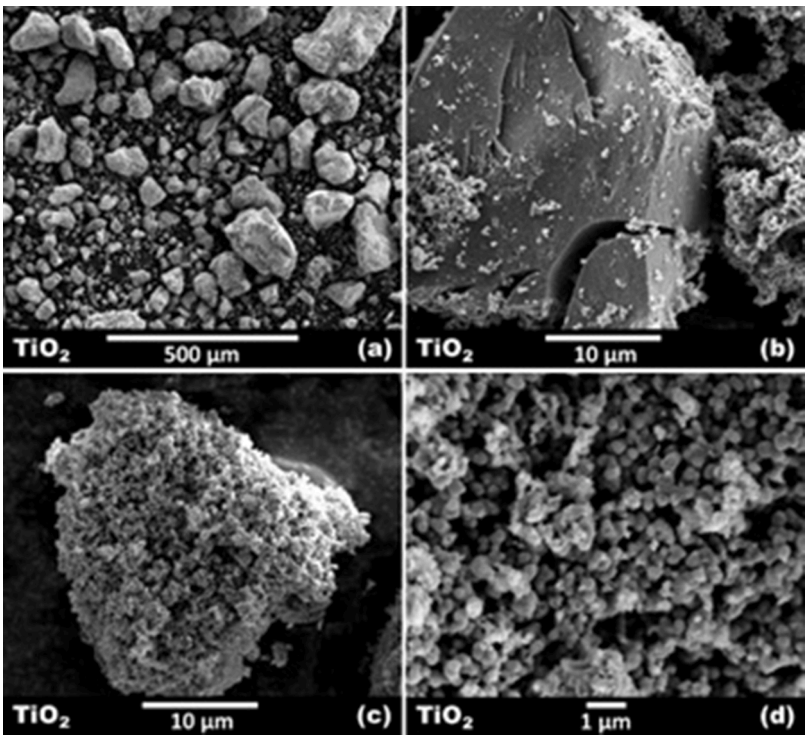

Fig. 1. SEM images of white TiO_2 powders.

Table 1
Elemental composition of powder samples.

	Elemental composition measured by EDS						
Sample	Ti	O	C	Na	B*	Trace elements (S, P, Si)	O:Ti ratio
TiO_2	34.0	56.7	9.3	–	–	–	1.7
B1	32.7	55.4	10.8	0.9	–	0.2	1.7
B2	34.3	54.6	9.9	1.1	–	0.1	1.6
B3	39.0	54.9	4.9	1.1	–	0.1	1.4
	Elemental composition measured by XPS						
	Ti	O	C	Na**	B	Trace elements (S, P, Si)	O:Ti ratio
TiO_2	24.8	58.7	16.5	–	–	<0.1	2.4
B1	23.2	56.2	14.9	4.9	0.8	<0.1	2.4
B2	20.2	53.4	16.1	7.0	3.2	<0.2	2.6
B3	19.3	52.8	14.5	8.5	4.8	<0.2	2.7

*Boron detection by EDS is technologically limited and intentionally was not executed

*Sodium concentration can be overestimated due to the partial overlap between the Na 1 s and Ti LMM Auger electron peaks.

$$2TiO_2 + hv \Leftrightarrow TiO_2\ (e^-) + TiO_2\ (h^+) \quad (1)$$

$$e^- + h^+ \Leftrightarrow 2TiO_2 + \text{heat} \quad (2)$$

$$h^+ + Red_1 \Leftrightarrow Ox_1^+ + TiO_2 \quad (3)$$

$$h^+ + H_2O \Leftrightarrow HO^\bullet + H^+ + TiO_2 \quad (4)$$

$$h^+ + HO^- \Leftrightarrow HO^\bullet + TiO_2 \quad (5)$$

$$e^- + O_2 \Leftrightarrow O_2^{-\bullet} + TiO_2 \quad (6)$$

$$O_2^{-\bullet} + H^+ \Leftrightarrow HO_2^\bullet \quad (7)$$

$$2HO_2^\bullet \Leftrightarrow O_2 + H_2O_2 \quad (8)$$

$$e^- + Ox_2 \Leftrightarrow Red_2^- + TiO_2 \quad (9)$$

Radicals and ions formed on the surface of the semiconductor participate in the following processes: a. react with adsorbed compounds on semiconductor materials; b. may diffuse from the surface of the semiconductor into solution by participating in chemical reactions; c. they can recombine; responsible for low photodegradation efficiency limited the applications.

There are some limitations of titanium oxide photocatalysts in the visible light application: (1) rapid recombination between electrons and holes (Eq. (2) and (2) titanium oxide adsorption only under UV radiation. Numerous studies are published yearly to elucidate these TiO_2 limits toward photocatalytic activity under visible light irradiation [13, 14].

Black TiO_2, usually called defective TiO_2, is a recently investigated material that exceeds these limits [15] by creating the defect species such as oxygen vacancies and Ti^{3+} [16] as described by the defect reaction (Eq. (10)); enhanced photocatalytic capacity [17,18]. Ti^{3+} species have been reported as colour centres leading to significant changes in the E_g value of TiO_2 [19] and electronic structure [20].

Table 2
The textural parameters (N_2 adsorption-desorption measurement), crystallite size and crystalline form (XRD), DLS characterisation, pH_{ZPC} and bandgap of materials.

Samples	N_2 adsorption-desorption				DLS				pH_{ZPC}	XRD		E_g (eV)
	S_{BET} (m^2/g)	Pore volume (cm^3/g)	Average pore size (nm)	Mean nanoparticle size (nm)	Z-average diameter (nm)	PDL	SIZE (nm)	VOLUME (%)		Crystallite size	Crystalline form	
TiO_2	34.69	0.078047	8.999	173	457	0.348	101.5 559 5278	1 49.7 49.3	6.45	29.9 nm 50.5 nm	Anatase Rutile	3.45
B1	37.68	0.097878	10.39	159	458.8	0.41	747.3 5389	68.3 31.7	6.485	25.5 nm 26.3 nm 13.9 nm	Anatase Rutile TiO_x	3.41
B2	32.518	0.080050	9.84	184.5	489.8	0.383	611.6 5163	40.2 59.8	6.4	28.3 nm 17.3 nm 15.3 nm	Anatase Rutile TiO_x	2.85
B3	33.5	0.090632	10.82	179.08	391.1	0.35	107.5 523.8 5338	1.9 56.4 41.8	6.94	23.1 nm 38.0 nm 7 nm	Anatase Rutile TiO_x	3.32

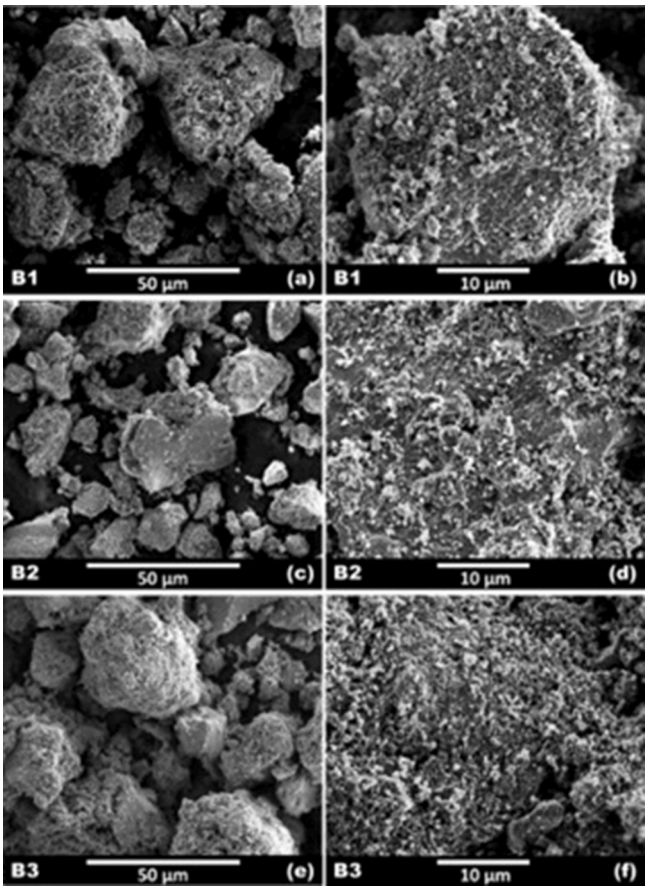

Fig. 2. SEM images of black TiO_2 powders.

$$2Ti_{Ti}^{x} + O_O^x \rightarrow 2Ti_{Ti}^{'} + 1/2O_2 + V_O^{\cdot\cdot} \quad (10)$$

Sodium borohydride ($NaBH_4$) can reduce Ti^{4+} to Ti^{3+} according to Eqs. (11) and (12) because H_2 is formed *in situ* at room temperature (Eq. (13)), and white TiO_2 turns to black powder and has Ti^{3+} vacancies [15].

$$NaBH_4 + 8OH^- \rightarrow NaBO_2 + 6H_2O + 8e^- \quad (11)$$

$$Ti^{4+} + e^- \rightarrow Ti^{3+} \quad (12)$$

$$BH_4^- + 2H_2O \rightarrow BO_2^- + 4H_2 \quad (13)$$

Getting a high concentration of surface defects on TiO_2 without impurities is still a big challenge. The presence of bulk oxygen vacancies in the TiO_2 lattice causes an increase in chemical potential in the region where bulk oxygen vacancies exist. In addition, surface defects play an important role in photocatalytic processes on the TiO_2 surface. The surface oxygen vacancies influence the photocatalytic activity under visible light and act as traps to inhibit electron-hole recombination [21]. During the annealing of photocatalytic materials, diffusion of oxygen vacancies from the bulk to the surface is possible, while oxygen ions diffuse into the TiO_2 bulk. Therefore, defects such as Ti^{3+} and oxygen vacancies coexist in the defective TiO_2, according to Eq. (14) [22].

$$O^{2-} + 2Ti^{4+} \rightarrow O_v + \frac{1}{2}O_2 + 2Ti^{3+} \quad (14)$$

The scavengers are assumed to react fast with a ROS species, inducing other stable species not implicated in the photocatalysis mechanism [23,24]. In this study, formic acid (20 mM), 2-propanol (1 M), 1,4 benzoquinone (1 mM), and potassium dichromate (1 mM) have been used as species for holes (Eq. (15)), hydroxyl radicals (Eq. (16)), superoxide ion radicals (Eq. (17)), and electrons scavengers (Eq. (18)) to prove the contribution of these species in the photocatalysis mechanism.

$$HCOO^- + h^+ \rightarrow CO_2 + H^+ \quad (15)$$

$$HO^{\cdot} + (CH_3)_2CH - OH \rightarrow H_2O + (CH_3)C^{\cdot} - OH \quad (16)$$

$$BQ + O_2^{\cdot -} \rightarrow BQ^{\cdot -} + O_2 \quad (17)$$

$$Cr_2O_7^{2-} + 14H^+ + 6e^- \rightarrow 2Cr^{3+} + 7H_2O \quad (18)$$

This work reports a systematic investigation of black TiO_2 nanoparticles for imidacloprid degradation under UV and simulated VIS irradiation for the first time. The different ratios between $NaBH_4$ and white TiO_2 were chosen to investigate Ti^{3+} and oxygen vacancies generation on the photodegradation of imidacloprid, in detail, a more convenient and economical synthesis method compared with other reported methods. Moreover, the scavengers effect on the degradation mechanism were investigated.

2. Experimental procedures

2.1. Black TiO_2 nanoparticles synthesis

Synthesis of black TiO_2 nanoparticles consists of the following steps: (1) TiO_2 sol-gel was obtained from titanium isopropoxide (≥97.0%, Sigma-Aldrich), as Ti precursor in nitric acid medium and calcinated at 500 °C for three hours, the temperature was chose based on previously our experiments to obtain mainly the structural form anatase and rutile [25,26]. In the second step, a chemical reduction of the TiO_2 sol-gel with $NaBH_4$ (sodium borohydride, 99%, VenPure) occurred. Powder of TiO_2 and $NaBH_4$ were mixed in a mass ratio of 4: 1 (denoted as B1), 2: 1 (B2)

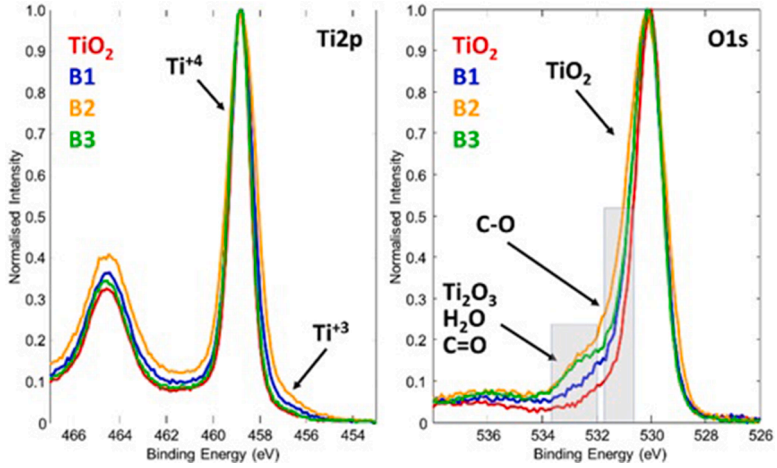

Fig. 3. Comparison of Ti2p and O1 s core level electron spectra.

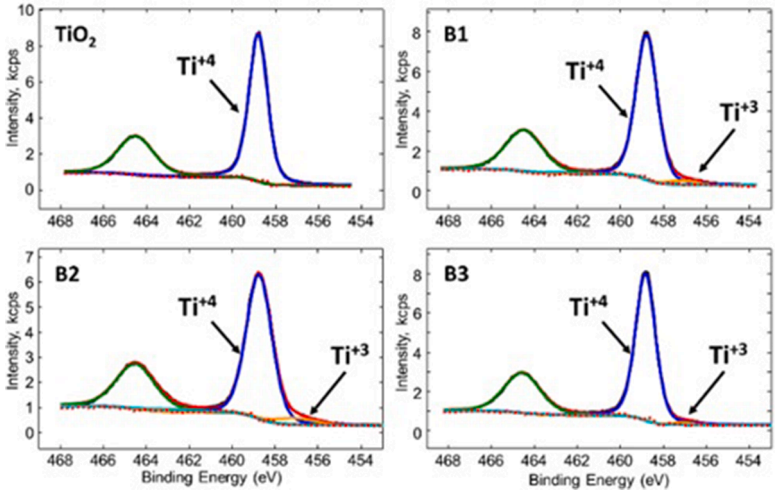

Fig. 4. Fitting of white and black TiO_2 powder Ti2p peaks.

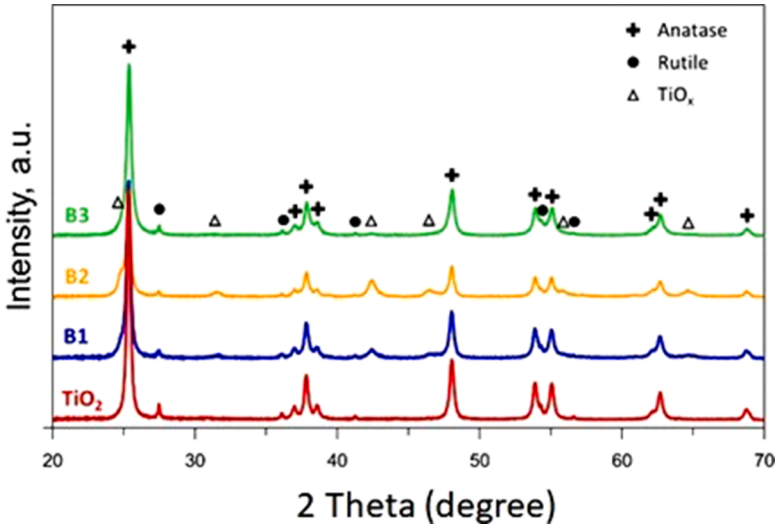

Fig. 5. XRD patterns of white and black TiO_2 powders.

and 1: 1 (B3), respectively. The powders were mixed, homogenised, and introduced in an oven at 350 °C for 1 h in the argon atmosphere (increasing temperature by 5 °C/min). They were then cooled to room temperature, washed with HCl 1 M solution, filtered many times until the pH reached around 6–7, and dried in a forced-air oven for 12 h at 105 °C. The powders synthesised by this method have a dark grey to

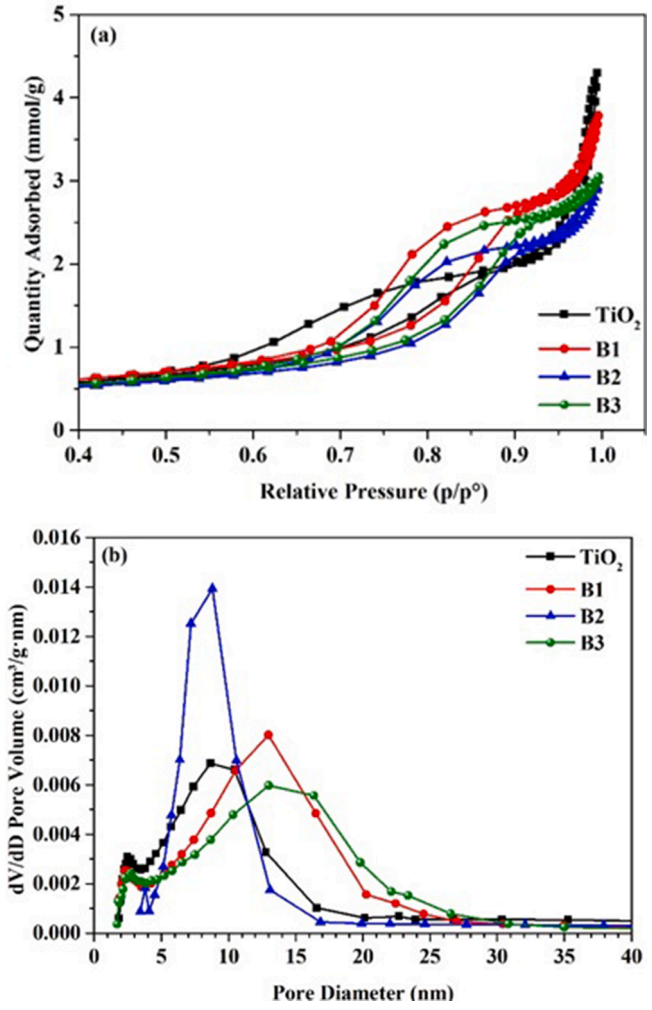

Fig. 6. (a) N2 adsorption-desorption isotherms and (b) BJH pore size distribution diagram of catalysts.

black appearance, depending on the TiO_2:$NaBH_4$ ratio used in the synthesis.

2.2. Photocatalysts characterisation

The X-ray diffraction was used to investigate the crystal structure of the samples, the XRD equipment Bruker D8 with theta-theta goniometer operation and Cu Ka radiation was used to obtain the patterns, and the crystallite size was evaluated using the TOPAS software package. Powder images and elemental composition were measured by Scanning Electron Microscope (equipment: Hitachi S-3400 N) equipped with Energy-Dispersive Spectrometer (equipment: Bruker Quad 5040). The chemical composition of the samples was evaluated using X-ray Photoelectron Spectrometer (equipment: PHI Versaprobe 5000) using monochromated Al Kα radiation (1486.6 eV). These measurements were performed using 25 W beam power, 100 μm beam size and 45° measurement angle. Sample charging was neutralised using a dual system consisting of low energy electrons and ions. As charge reference, adventitious carbon C1s peak position of 284.8 eV was used. A diffuse reflectance measurement and Kubelka-Munk model were utilised to determine the band gap value of the materials. The particle size distribution is an important parameter to study; freshly prepared samples in distilled water were analysed using the dynamic light scattering (DLS) method, analysed Zetasizer Nano ZS. Zetasizer Nano ZS has been used to measure smaller particles ranging from 0.6 nm to 10 μm. Triplicate measurements were taken from diluted particle suspensions (10 mg/10 mL distilled water) after 5 min of sonication. Three replicate samples per time point were performed, and the data were shown as mean. The data for DLS is represented as volume frequency (%).

N_2 adsorption-desorption isotherms for synthesised materials were obtained at −196 °C (equipment: Micromeritics Tristar II Plus analysers) after outgassing 4 h at 250 °C under vacuum (10^{-3} Pa). The measurement provides the surface area and porosity measurements.

The mass titration method determined the zero point charge of TiO_2 and black TiO_2, and was experimentally done by acid-basic titration, previously described [27,28]. As a result, the graphical representation of V_{total} of acid as a function of pH, and by deriving the first order of the graph (Fig. 1S), the values for isoelectric pH were obtained.

2.3. Photocatalytic experiments

The photocatalytic activity of materials was evaluated by investigating the degradation of imidacloprid under UV and UV–VIS irradiation at room temperature. Different quantities of photocatalysts (0.6 and 1 g/L) were added to 50 mL of IMD (20 mg/L) with unmodified pH, for two reasons: (1) a concentration of 1 g/L was used to investigate the photocatalytic efficiency of the synthesized materials as a function of irradiation time and (2) a concentration of 0.6 g/L was chosen to highlight the effect of ROS on the photodegradation mechanism of imidacloprid. The suspension was magnetically stirred in the dark for 30 min to achieve adsorption-desorption equilibrium between IMD and the photocatalyst. Ten tubes of Philips F18W/T8 black light and UVA light (340–400 nm, λ_{max} = 365 nm, 180 W) provided the UV irradiation. The simulated solar irradiation (excluding IR) consists of 80% VIS and 20% UV provided by 8 Philips TL-D Super 80 18 W/865 tubes, Vis light (400–700 nm, λ_{max} = 565 nm, 144 W) and two tubes Philips F18W/T8 black light (nominal power of 36 W). The sample was taken every 30 min for 6 h, centrifuged at 2000 rpm for 5 min, and filtered through Millex 0.45 μm filters. The supernatant concentrations were analysed using high-pressure liquid chromatography (HPLC). The Shimadzu LC-20ADsp instrument is equipped with a UV detector SPD-20A and set at a wavelength of 270 nm, a C18-Macherey Nagel column, Nucleosil 5 μm, the mobile phase was acetonitrile: water (70:30), and flow was 1.2 mL/min. The HPLC method was developed and validated in terms of linearity, range, the limit of quantification (LOQ) and the limit of detection (LOD) using a series of standard solutions between 5 μg/L and 100 mg/L. The degradation rate of IMD was calculated using Eq. (19).

$$\eta = \frac{C_0 - C}{C_0} \cdot 100 \tag{19}$$

where: c_0=initial IMD concentration (mg/L), and c=IMD concentration (mg/L) at a time t (minute).

Preliminary studies were performed in the absence of the photocatalyst in the dark, indicating that IMD has good photochemical stability and the absence of photolysis processes. Furthermore, the photolysis mechanism (only pollutant under illumination conditions) does not significantly affect the photodegradation tests.

All experiments indicated pseudo-first-order photodegradation kinetic (Eq. (20)) concerning the IMD concentration and modelled by the Langmuir–Hinshelwood relation (Eq. (21)), which allows determining the values of the kinetic constants (k, min^{-1}) and the half-life ($t_{1/2}$) when half of IMD concentration is degraded (Eq. (22)).

$$c = c_0 \cdot e^{-k \cdot t} \tag{20}$$

$$ln c/c_0 = -kt \tag{21}$$

$$t_{1/2} = \frac{\ln 2}{k} \tag{22}$$

The scavengers effect was investigated to elucidate the photodegradation mechanism of imidacloprid over nanoparticles photocatalyst. The reaction was accomplished with an aqueous solution of

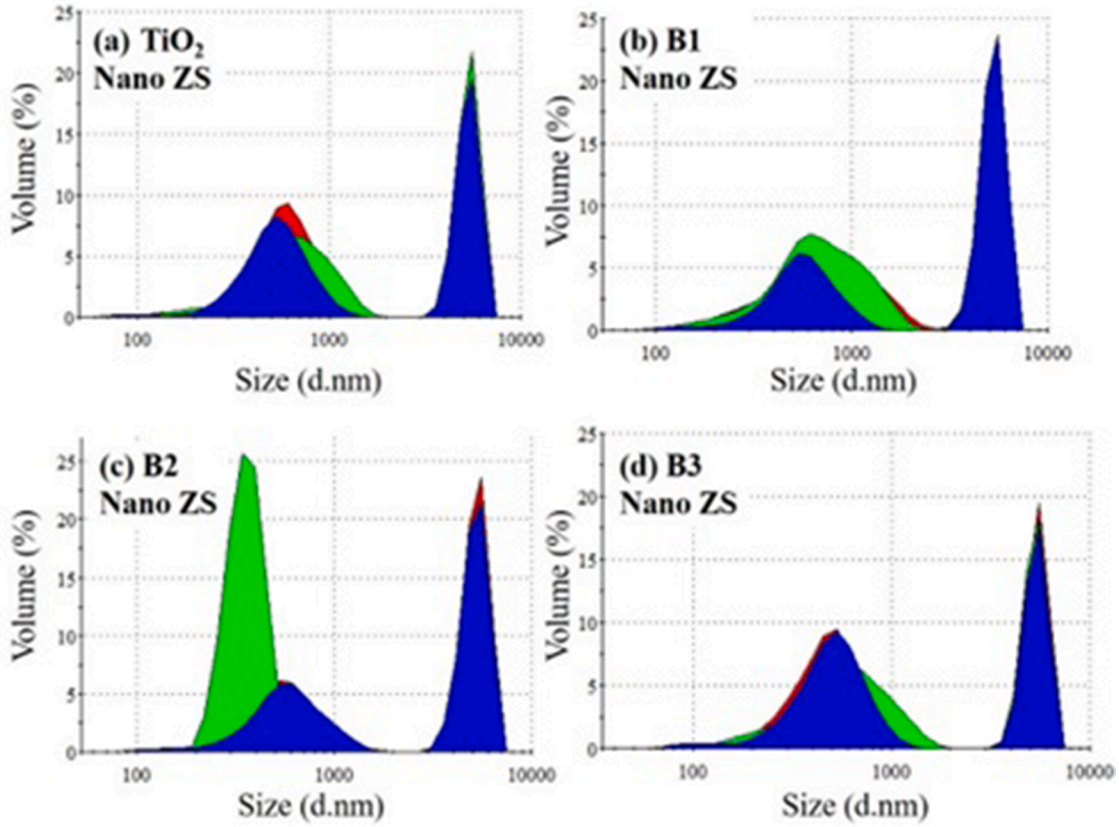

Fig. 7. Particle size distribution examined by DLS measurements. Particles size between 0.6 nm and 10 μm, represent as volume frequency (%) produced by irradiation of a solution of 10 mL distilled water containing 10 mg nanoparticles of TiO2 (a), B1 (b), B2 (c) and B3 (d) respectively.

imidacloprid 20 mg/L containing 0.6 g/L photocatalysts for up to six hours and with the addition of scavenging species, formic acid (20 mM), 2-propanol (1 M), 1,4 benzoquinone (1 mM), and potassium dichromate (1 mM) for holes (Eq. (15)), hydroxyl radicals (Eq. (16)), superoxide ion radicals (Eq. (17)), and electrons scavengers (Eq. (18)).

3. Results and discussions

3.1. Materials characterisation

EDS and XPS techniques analysed the elemental composition of white and black powders (Table 1). EDS technique obtains most of its signal from the depth of 1–2 μm and provides a more generalised composition of the powders. In contrast, XPS is a surface analysis technique and provides information only from the top 5–10 nm. Unfortunately, both methods can not warranty high quantitative precision. Nevertheless, their combination can provide valuable qualitative insights into the difference between the „bulk" and the top surface of the powders.

EDS analysis revealed that O:Ti ratio for the white TiO_2 powder sample was approximately 1.7. Slightly sub-stoichiometric O:Ti ratio of TiO_2 powder produced by sol-gel is not extraordinary and can be present if 500 °C annealing temperature is used [29]. Theoretically, TiO_2 reduction by $NaBH_4$ Eqs. (1) and ((2) should partly change the oxidation state of titanium from +4 to +3 and create oxygen vacancies. In practice, these reactions are reflected by shrinking the O:Ti ratio, which decreased from 1.7 to 1.6 and 1.4 as TiO_2:$NaBH_4$ ratio was 4:1, 2:1 and 1:1, respectively.

Interestingly, O:Ti ratios measured by XPS demonstrate a completely opposite tendency to the values provided by EDS. First, O:Ti ratio for all samples is higher than the stoichiometric value. Second, the O:Ti ratio increases as a higher quantity of $NaBH_4$ is used for the reduction. In general, the over-stoichiometric O:Ti ratio obtained by XPS can be explained entirely by the peculiarities of the method. XPS obtains information from the top surface; therefore, its data combines the signal coming from the sample and adventitious contamination composed of various hydrocarbons and moisture. In the current study, before XPS analysis, samples were handled in air, which is the main source of the observed carbon and additional oxygen (in EDS study, most of the carbon signal was observed from the carbon conductive tabs which were used for the powder placement).

While the reasoning behind stoichiometry discrepancy is relatively straightforward, the nature of different O:Ti ratio trends for "surface" and "bulk" is unambiguous. To understand it, we compared Ti2p and O1s core level electron spectra (Fig. 3) and looked for surface chemistry changes. Main $Ti2p_{3/2}$ peaks for all samples were positioned at 458.8 eV, and corresponding $Ti2p_{1/2}$ peaks were placed at 464.5 eV. Position of the peaks, duplet separation energy (5.7 eV), and high peak symmetry (Fig. 4) [30] confirmed that at the surface of white TiO_2 powder, nearly all titanium was fully oxidised to Ti^{+4} state. Detailed analysis of black powder Ti2p spectra (Fig. 4) identified additional weak peaks at approximately 457.1 eV and 462.8 eV which are attributed to the Ti^{+3} state [31]. Mathematical fitting revealed up to 3%, 6%, and 2% of titanium at the surface in Ti^{+3} oxidation state, for samples B1, B2, and B3, respectively. Combined with EDS data, these numbers suggest that "bulk" and "surface" regions of black TiO_2 powder are not uniform. The bulk has many oxygen vacancies, whereas its surface is nearly fully oxidised. Presumably, limited oxidation of TiO_2 surface could have taken place during their drying at 350 °C. O1s spectra of white TiO_2 powder has the main peak located at 530.0–530.1 eV. This peak well corresponds with the reported values of TiO_2 [32]. A small shoulder peak at approximately 531.0–531.5 eV can be attributed to the C-O [33]

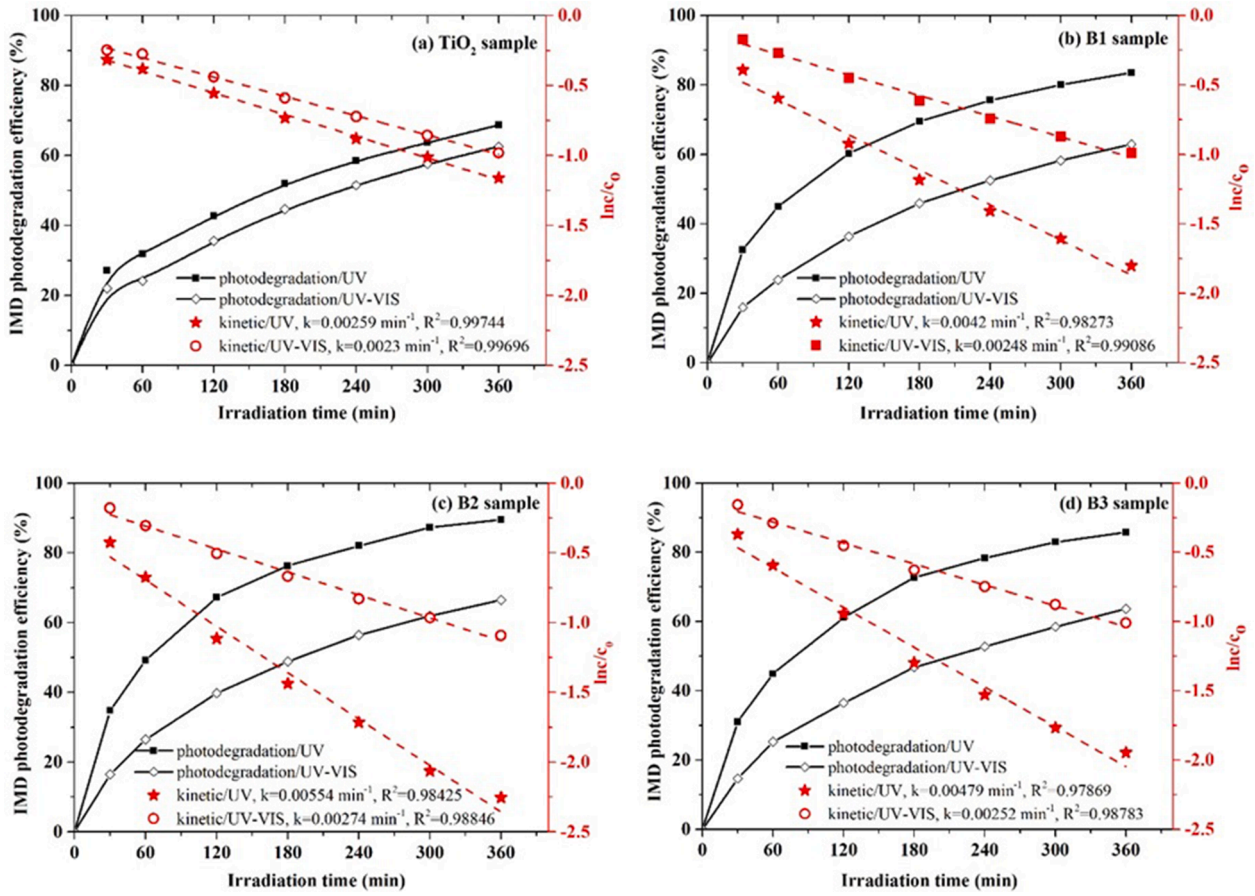

Fig. 8. The photocatalytic efficiency (black line) and the first-order degradation kinetic (red line) of materials (a) TiO2 sample, (b) B1 sample, (c) B2 sample, and (d) B3 sample. (Experimental conditions: photocatalyst 1 g/L, IMD 20 mg/L). (For interpretation of the references to colour in this figure legend, the reader is referred to the web version of this article.)

Table 3
Photodegradation rate constants and half-lives of IMD in two photocatalyst concentrations (1 g/L and 0.6 g/L) and under two irradiation types (UV and UV-VIS).

Samples	k (min^{-1})	$t_{1/2}$ (h)	R^2	k (min^{-1})	$t_{1/2}$ (h)	R^2	k (min^{-1})	$t_{1/2}$ (h)	R^2	k (min^{-1})	$t_{1/2}$ (h)	R^2
	$C_{photocat}$=1 g/L,UV irradiation			$C_{photocat}$=0.6 g/L,UV irradiation			$C_{photocat}$=1 g/L,UV–VIS irradiation			$C_{photocat}$=0.6 g/L,UV–VIS irradiation		
TiO_2	0.00259	4.46	0.99744	0.00362	3.19	0.96984	0.0023	5.02	0.99696	0.00168	6.88	0.99744
B1	0.00421	2.74	0.98273	0.00214	5.40	0.94756	0.00248	4.66	0.99086	0.00173	6.68	0.98964
B2	0.00554	2.09	0.98425	0.00184	6.28	0.8623	0.00274	4.22	0.98846	0.00194	5.95	0.9867
B3	0.00479	2.41	0.97869	0.00234	4.94	0.99183	0.00252	4.58	0.98783	0.00166	6.96	0.98917

or O-H groups [34]. Reduced samples have a significantly stronger shoulder extended towards higher binding energies. According to literature, O1s components at 532.0–532.5 eV can be attributed to the adsorbed water moisture, C=O, and Ti_2O_3 [30]. However, considering relatively small fractions of observed Ti^{+3} and low probability of carbonate formation, we assume that most of the surplus oxygen is brought up by the adsorption of water moisture. It can be noticed that reduction by $NaBH_4$ increases the surface area of black TiO_2 powders, which is a potential booster for moisture adsorption. Accordingly, it would explain the increased O:Ti ratio trend observed by XPS but not by EDS analysis (Table 1).

XRD patterns of white and black powders are presented in Fig. 5. Titanium oxide forms anatase and rutile phases mixture in all samples, where anatase fraction is approximately 94–96%. In addition to the stoichiometric titanium dioxide phases, samples B1, B2, and B3 also have several relatively wide peaks which were not fully matched by any of the titanium-oxygen compounds included in the comprehensive PDF-4 + 2022 Powder Diffraction File database. The unknown phase did not correspond to the database's titanium or sodium oxide, borate, hydride or hydroxide phase. On the other hand, it can be noticed that the intensity of the unknown phase well correlates with the intensity changes of Ti^{+3} peaks in XPS spectra (Fig. 4). Moreover, all but one peak of the unknown phase was matched by the PDF pattern #01–071–6414, attributed to the orthorhombic $Ti_{4.5}O_5$ oxide. Considering these two factors, we assume that reducing white TiO_2 powder resulted in some crystalline titanium suboxide phase formation. Synthesis of such suboxide phase would agree with EDS data presented above. Crystallinity determination is complicated with an unknown phase because it is not clear which features belong to this possible TiO_x phase. More quantitative details of the observed phases and their distribution are provided in Table 2.

The detailed experimental data related to the BET surface area, porosity, volume of pores, pore size and nanoparticle size were calculated by the BJH method and are listed in Table 2 to explore the effect of pore structure and surface area on IMD photocatalysis. The specific BET surface area and pore size slightly vary after reduction, in which the surface area, pore size and pore volume of TiO_2 sample were 34.69 m^2/g, 8.999 nm and 0.078 cm^3/g, respectively, then increased in B1 sample

Table 4
Comparison of the photocatalytic performance between defective black TiO_2 materials.

Pollutant/category	Photocatalyst: Synthesis method and experimental conditions	Properties	Irradiation source	Experimental condition	Photodegradation efficiency, kinetics	Refs.
Imidacloprid (pesticide)	sol-gel followed by $NaBH_4$ reduction, 350 °C, 1h	S_{BET} =32.518 m^2/g E_g=2.85eV	UV - Philips UV-B tubes (180 W) UV–VIS – 144 W Philips TL-D tubes and UV-B tubes 36W	Catalyst = 1 g/L IMD=20 mg/L	90%, 360 min, UV, k = 0.00554 min^{-1} 67%, 360 min, UV–VIS, k = 0.00274 min^{-1}	This work
Gallic acid (phenolic compound)	green chemical precipitation synthesis using glycerol as a reducing agent	S_{BET} =99.98 m^2/g E_g=2.67eV	500 W halogen lamp	Catalyst = 16 g/L GA=224.85 mg/L	48.17%, 3 h, VIS	[45]
Tetracycline (pharmaceuticals)	H_2 treatment p = 5 bar, 24 h, 400 °C	S_{BET} =22.2 m^2/g	1000 W Xe lamp, 400 nm cut-off filter (40 mW cm^{-2})	Catalyst=0.2 g/L TC= 10 mg/L	66.2%, 4 h, VIS, k = 0.0045 min^{-1}	[46]
Acetaminophen (pharmaceuticals)	H_2 atmosphere, flow of 100 mL/min, for 3 h at 500 °C	S_{BET} =40.62 m^2/g E_g=2.53eV	A 150 W Xe arc lamp	Catalyst: pellet ACE= 1 mg/L	90%, 3 h, VIS, k = 0.998 h^{-1}	[47]
Rhodamine B (dye)	the evaporation-induced self-assembly followed by $NaBH_4$ reduction	S_{BET} =233 m^2/g	300 W Xe lamp, 400 nm cut-off filter	Catalyst =0.006 g/L RhB=0.005 mM	93%, 50 min, VIS,k = 0.038 min^{-1} 90%, 10 min, UV, k = 0.236 min^{-1}	[48]
Rhodamine B (dye)	hydrothermal synthesis method, 180 °C for 12 h, ascorbic acid as reductant	E_g=2.54 eV	300-W Xenon lamp	Catalyst = 0.4 g/L RhB=5 mg/L	57.8%, 180 min, VIS,k = 0.0031 min^{-1}	[49]
Rhodamine B (dye)	sol–gel hydrothermal method, 200 °C for 1 h	S_{BET} =173.6 m^2/g	300 W Xe lamp, 400 nm cut-off filter	Catalyst = 1 g/L RhB=20 mg/L	99%, 20 min, VIS	[50]
Methyl orange (dye)	sol-gel TiO_2 by $NaBH_4$ reduction 500 °C for 10 h, $NaBH_4$: TiO_2 = 1:1 (molar ratio)	S_{BET} =42.4 m^2/g E_g=1.7 eV	UV 0.044 W/m^2, (75 W Philips) VIS, 0.291 W/m^2, (18 W Philips TL-D standard colour lamp)	Catalyst = 1 g/L MO=10 mg/L	82.17%, 4 h, UV 71.92%, 4 h, VIS	[51]
Methyl orange (dye)	Anatase TiO_2 powder and aluminium reduction, 650 °C 60 min	E_g=2.5eV	300 W Xe lamp, cut-off filter ($\lambda > 420$ nm)	Catalyst = 0.5 g/L MO=500 mg/L	56%, 120 min, VIS, k = 0.334 h^{-1}	[52]
methylene blue (dye)	colourful defective tio_{2-x} microspheres solvothermal method	S_{BET} =255.4 m^2/g E_g=2.16 eV	300 W Xe lamp, 400 nm cut-off filter	Catalyst = 2 g/L MB= $2{\cdot}10^{-5}$ M	90%, 1 h, VIS	[53]
Methylene blue (dye)	black TiO_{2-x} microspheres, ultrasonic spray pyrolysis, 900 °C	E_g=2.82 eV	300 W Xe lamp and Air Mass 1.5 Global Filter	Catalyst = 1 g/L MB= $2{\cdot}10^{-5}$ M	78%, 2 h, VIS, k = 0.01040 min^{-1}	[54]

IMD=imidacloprid, GA= gallic acid, TC=tetracycline, ACE=acetaminophen, RhB=Rhodamine B, MO=methyl orange, MB=methylene blue.

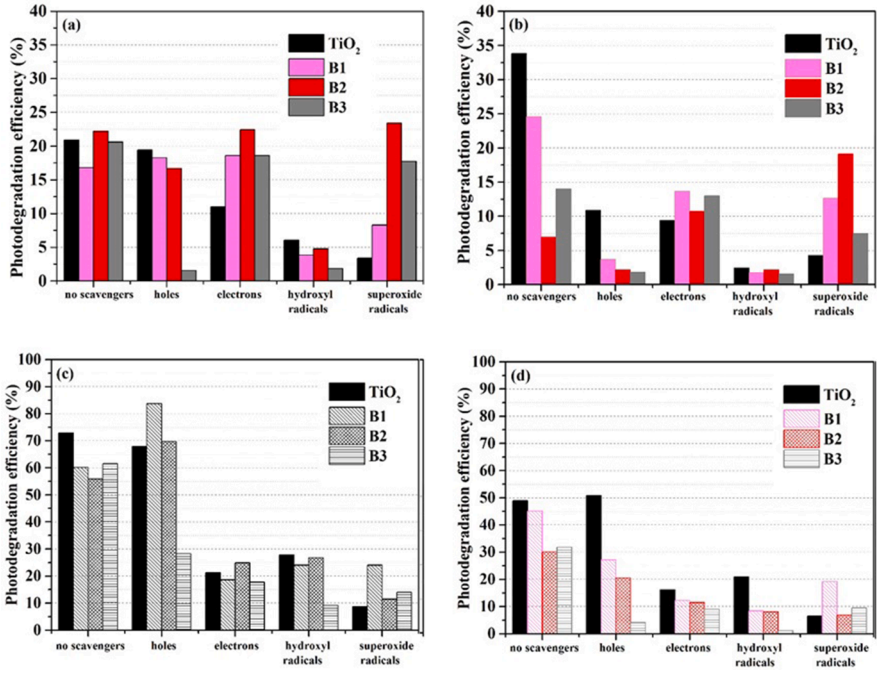

Fig. 9. Effect of holes, electrons, hydroxyl radicals and superoxide radicals scavengers on photocatalytic degradation of IMD under UV, 1 h (a) and 6 h (c) and UV–VIS, 1 h (b) and 6 h (d) irradiation (Experimental conditions: photocatalyst 0.6 g/L, IMD 20 mg/L).

at 37.68 m^2/g, 10.39 nm and 0.097 cm^3/g, respectively, indicating a large number of interconnected fine TiO_2 nanoparticles, observed in SEM analysis (Fig. 2) rendering the generation of oxygen vacancies exhibit a high photocatalytic activity (Fig. 8).

The catalysts' N_2 adsorption and desorption isotherm curves and the pore size distribution plots obtained by BJH are shown in Fig. 6a and

Table 5
The significance of active species in the imidacloprid photodegradation pathway.

Catalysts	Photodegradation mechanism							
	UV irradiation (6 h)				UV–VIS irradiation (6 h)			
	holes	electrons	hydroxyl radicals	superoxide ion radicals	holes	electrons	hydroxyl radicals	superoxide ion radicals
TiO_2	×	❖	❖	✓	×	❖	❖	✓
B1	×	✓	❖	❖	❖	✓	✓	❖
B2	×	❖	❖	✓	❖	✓	✓	✓
B3	❖	❖	✓	✓	✓	✓	✓	✓

× The scavenger influence on the degradation efficiency is insignificant or missing
✓
The scavenger influence on the degradation efficiency is significant
❖
The scavenger influence on the degradation efficiency is average
h^++IMD → intermediates/mineralisation products.
$e^- + O_2 \rightarrow {}^{\cdot}O_2^-$
${}^{\cdot}OH$ + IMD → intermediates/mineralisation products.
${}^{\cdot}O_2^-$+IMD→ intermediates/mineralisation products

Fig. 6b, respectively. As shown in Fig. 6a, all the samples belong to the same shape as a type IV isotherm, which has a clear H4 hysteresis loop for TiO_2 and H3 hysteresis loop for black TiO_2, appearing at high relative pressure p/p_0=0.6–0.9, characteristic of mesoporous materials [35], indicating that the samples have narrow mesopores, which is beneficial for exposure organic pollutants of more active sites [36]. On the other hand, the reduced black TiO_2 (B1, B2 and B3) hysteresis loop at a higher pressure (p/p_0 0.8 to 0.9) reflected the structural defects formed during the reduction process. In Fig. 7, the pore distribution of samples shows the highest peak value at 8.77 nm, 13.19 nm, 8.95 nm and 12.43 nm, respectively, corresponding to TiO_2, B1, B2 and B3, that it has mainly mesopores as reported in the literature [37], suitable for effective diffusion of imidacloprid molecules (5.9 Å) into channels and provide accessibility to the active sites.

The dynamic light scattering (DLS) measurements assume that all particles are spherical. However, most of the particles studied in this paper are not spherical and scatter the light differently depending on its orientation. Furthermore, since the measurements are performed for particles in DI water, the particles in the solution are arbitrarily floating around, and the error source is random. The aggregates of TiO_2 nanoparticles suspended in water were determined using DLS measurements (Nano ZS) (Fig. 7) under three conditions: (1) after 5 min of ultrasonic treatment (designed red in the graph, as immediate particle size), (2) 3 min (designated as green) (3) 6 min (designated as blue) after the experiment was started. The measurement shows TiO_2 nanoparticles consist of aggregates with a Z-average diameter of 457 nm, with the main contribution of 49.7% of the particles of 559 nm, 49.3% of 5.278 μm in diameter. In suspension in distilled water, black TiO_2 Z-average diameter was 458.8 nm (B1 sample), 489.8 nm (B2 sample) and 391.1 nm (B3 sample), respectively, as shown by DLS technique (Table 2, Fig. 7). The aggregates between 400 nm and 5 μm were also observed in the SEM images (Figs. 1 and 2).

The isoelectric point of the materials is another quantity of parameters that influences the photodegradation processes of pollutants. At pH values lower than pH_{ZPC}, the surface becomes positively charged, while at pH> $pH_{ZPC,}$ the surface becomes negatively charged. Consequently, in acidic solutions (the pH of the imidacloprid solutions used in the photodegradation tests was 6.35), due to the existence of electron-rich aromatic rings in the structure of the imidacloprid molecule, it tends to be adsorbed on the positively charged surface of the powders. Synthesised, thus from an electrostatic point of view, all materials are charged favourably (positively) at the pH of the pollutant (6.35), favouring the photodegradation reactions, a fact confirmed by the very good photodegradation efficiencies (Fig. 8). Imidacloprid is a pesticide whose pKa are 1.56 and 11.12 [38]. The pH_{PZC} were around 6.4 … 6.94 (Table 2) and above 6.35 characteristic of imidacloprid at which photocatalysis takes place, favouring the degradation reaction by electrostatic interactions established between the pollutant molecules and the surface of the photocatalyst (Table 2S). On the other hand, when working at pH < pH_{PZC}, the catalyst surface becomes positively charged, and there are repulsive forces between the positively charged surface of the IMD. Therefore, an attraction between photocatalyst surface and contaminant molecules begins at pH values higher than pH_{PZC}.

3.2. Photocatalytic degradation of imidacloprid

The potential application of as-prepared black TiO_2 samples was evaluated for imidacloprid photodegradation as an environmentally friendly technology, under UV and UV-VIS irradiation, after various time intervals. The detection of imidacloprid was performed using a series of standard solutions. The calibration curve showed linearity in the concentration ranges 5 μg/L-100 mg/L with correlation coefficients of 0.9999. The LOD and LOQ were 50 μg/L and 160 μg/L, respectively. The regression equation for imidacloprid residue detection is y=45851x+8003.8, with a correlation coefficient R^2=0.9999.

The IMD degradation was under 3% in the photolysis experiments, which indicates the stability of IMD under UV and simulated visible light irradiation and without the presence of a photocatalyst. At an optimal photocatalyst concentration, a more significant number of active centres at the catalyst surface were available for more pollutant molecules. Thus, the degradation rate increases, which is characteristic of heterogeneous photocatalysis and agrees with the studies reported earlier [17, 39–43]. The effect of initial catalyst concentration was investigated under 0.6 and 1 g/L. For example, white titanium dioxide shows the best photodegradation efficiency of IMD under UV radiation if 0.6 g/L photocatalysts were used; increasing this amount to 1 g/L leads to a decrease in efficiency from 73% to 68%. As shown in Fig. 8, the degradation efficiency of IMD associated with B1, B2 and B3 photocatalysts reached 83%, 90%, and 86%, respectively, in 360 min, compering with only 68% in the presence of white TiO_2 photocatalyst, under UV irradiation. However, this difference between white and black TiO_2 is neglected under simulated visible irradiation, and only the B2 sample showed higher degradation efficiency of 67%.

The almost organic compounds followed the Langmuir-Hinshelwood kinetics. At very low concentrations of the pollutant, as run in this study, the kinetics is respect to pseudo-first-order. Table 3 shows that the most effective catalyst for IMD degradation was B2 applied with a concentration of 1 g/L under UV irradiation with a highest kinetic constant of 0.00554 min^{-1} consequently, the shorter half-life time 2.09 h. The same photocatalyst shows the best photocatalytic activity under UV-VIS radiation. The IMD half-life decreases from 4.46 h for TiO_2 to 2.41 for B1, 2.09 h for B2, 2.74 for B3, respectively, when the photocatalyst is in concentration 1 g/L, under UV irradiation. The narrow bandgap of black TiO_2 (sample B2), 2.85 eV lower than white TiO_2 3.45 eV (Table 2), confirms the most significant IMD degradation after 6 h of irradiation, around 90% under UV and 67% under UV-VIS irradiation, respectively.

The best photocatalytic activity of this material is associated with greater absorption of radiation due to the lower bandgap energy of all synthesised materials. The surface Ti^{3+} defects and oxygen vacancies in the B2 sample repressed the recombination of charge carriers, resulting in the highest photocatalytic activity [44].

The kinetic behaviours of photocatalytic degradation of IMD were also studied for synthesised photocatalysts by the Langmuir-Hinshelwood kinetic model, given in Eq. (20). Fig. 8 shows the linear relations between ln c/c_0 and irradiation time t, indicating that IMD degradation follows pseudo-first-order kinetics. The degradation rate constants of IMD increase to 0.00259, 0.0042, 0.00479, and 0.00554 min^{-1}, over the white TiO_2, B1, B3 and B2, respectively, after 6 h of UV irradiation (Fig. 8). In addition, the B2 sample displayed the best photocatalytic activity, which is almost two times higher than the white TiO_2 photocatalysts, respectively. Under simulated visible light irradiation, the degradation rate slowly increased in the following order TiO_2 (white)>B1>B3>B2. The results revealed that the activity of the B2 nanoparticles is two times greater under UV than simulated UV-VIS irradiation. Therefore, it can be noticed that the black TiO_2 nanoparticles show an increase in photocatalytic activity relative to white TiO_2, and the prepared nanoparticles can have a suitable application in photocatalytic processes.

Finally, we compared the photocatalytic performance of the materials synthesised in this work with other black TiO_2 materials, and the outcomes are provided in Table 4.

3.3. Effect of holes, hydroxyl radicals, superoxide ion radicals and electrons scavengers on photodegradation mechanism

In situ trapping, experiments were conducted to investigate species generated during photocatalysis of imidacloprid under settled conditions: IMD concentration 20 ppm, catalyst dosage 0.6 g/L. Upon UV adsorption, electrons are excited from the VB to the CB; the holes remain in the VB and could facilitate imidacloprid photodegradation, leading to their degradation to form inorganic such as NO_3^-, NH_4^+, CO_2 and H_2O. The process of recombining electrons and holes is a process that diminishes the efficiency of photodegradation. Thus, the addition of HCOOH as a hole scavenger leads to an increase in the degradation efficiency of IMD, allowing electrons to migrate to the catalyst surface and react with O_2 to form $O_2^{\cdot-}$ (Eq. (6)). These results indicate that superoxide radicals are the key species for IMD photodegradation. The increase in the photodegradation efficiency of IMD in the presence of hole scavengers is partly due to the capture of holes by the HCOOH (Eq. (14)), allowing electrons to participate in reduction reactions. Thus, the recombination reaction between holes and electrons no longer takes place. If the electrons and the holes are separated promptly, then the electrons on the surface can turn into superoxide radicals, and the holes turn into hydroxide radicals.

After 1 h of IMD degradation under UV irradiation (Fig. 9a), scavengers' presence decreases the photodegradation efficiency, which means there is a competition between ROS formation from the beginning of the photodegradation reaction. IMD photodegradation after one hour is between 17 and 22% for all materials without scavengers. An important role in this time interval is attributed to hydroxyl radicals, considered the dominant ROS in the photocatalytic systems, for white TiO_2 and black TiO_2 [55]. The role of reactive oxygen species (ROS) in the photodegradation mechanism of IMD after 6 h of UV irradiation in the presence of white TiO_2 decreases in order $O_2^{\cdot-} > e^- > HO^{\cdot} > h^+$ (Fig. 9c). Superoxide radicals have a minimum effect in the IMD photodegradation in the first 120 min, then their role increases due to their formation in Eq. (6), the degradation efficiency decrease in the presence of 1,4 benzoquinone. Additionally, other reactive species are formed on the photocatalyst's surface [56].

A reasonable mechanism of IMD degradation over black TiO_2 is presented in Fig. 9. Oxygen vacancies produce a donor state below the CB, which has promoted the visible-light response and charge transport property and captured the photogenerated electrons from VB. The electrons diminish the O_2 to ($O_2^{-\bullet}$) with a strong oxidation capacity, having an important role in the imidacloprid degradation mechanism.

A summary of the importance of the species generated in the photocatalysis process is presented in Table 5. Generation of superoxide anion, hydroxyl radicals and electrons are competitively contributing to the imidacloprid photodegradation, especially under simulated VIS irradiation and black TiO_2 as photocatalyst. The main active species in the IMD photodegradation are the hydroxyl radicals, especially under simulated VIS irradiation. In addition, the oxygen defects formed at the black titanium oxide surface can react with oxygen molecules adsorbed at the photocatalyst surface and generate more superoxide radicals.

4. Conclusions

The synthesis of nanomaterials with applications in the degradation of pollutants from wastewater, efficient in the presence of solar radiation, through a cheap, energy-efficient and large-scale production, remains a great challenge. We report a facile synthesis method of black TiO_2 that shows an enhanced performance compared to the pristine white TiO_2, and the photocatalytic performance was explored for imidacloprid degradation with enhanced VIS activity. Remarkably photocatalytic activity of black TiO_2 under visible light can be associated with the synergistic effect of specific surface area, bandgap energy smaller than white TiO_2, a large amount of surface defect Ti^{3+} and oxygen vacancies promote charge carriers' separation. A reduced bandgap value from 3.45 to 2.85 eV enhanced absorption of the visible light and thus increased the IMD degradation. The degradation mechanism of IMD over white and black TiO_2 photocatalysts was investigated in the presence of different radical scavengers as active species trapping. As a result, the degradation efficiency of IMD was significantly decreased with the addition of superoxide anions scavenger after 120 min of irradiation, which demonstrates that superoxide radicals were the main reactive species that participate in the IMD photocatalytic degradation. The degradation efficiencies in the presence of hydroxyl and electron scavengers were similar to superoxide, revealing that $HO^{\cdot}$ and e^- together with superoxide ROS played an essential role in the photodegradation reaction. However, the IMD degradation efficiencies in the presence of h^+ scavengers were similar in the absence of scavengers, indicating that h^+ has a minor role in the mechanism.

Declaration of Competing Interest

Luminita ANDRONIC reports financial support was provided by Transilvania University of Brasov. Martynas LELIS reports financial support was provided by Lithuanian Energy Institute. Smagul KARAZHANOV reports financial support was provided by Institute for Energy Technology. Alexandru ENESCA reports financial support was provided by Transilvania University of Brasov.

Acknowledgements

This work was completed in the "Theoretical and experimental study of transition metal oxyhydride nanomaterials for superconductivity and photocatalysis" project, acronym TESTIMONIES. Dr. Andronic Luminita and Dr. Enesca Alexandru were supported by a grant from the Romanian National Authority for Scientific Research and Innovation, CCCDI-UEFISCDI, Project No. 114/2019 ERANET-M.-TESTIMONIES, within PNCDI III. Dr. Martynas Lelis has received financial support from the Research Council of Lithuania (LMTLT), agreement No S-M-ERA.NET-19–1/18–1924.19.22. Dr. Smagul Karazhanov has received funding from the Research Council Of Norway Through Project No. 300107.

Supplementary materials

Supplementary material associated with this article can be found, in the online version, at doi:10.1016/j.surfin.2022.102123.

References

[1] T. Tisler, A. Jemec, B. Mozetic, P. Trebse, Hazard identification of imidacloprid to aquatic environment, Chemosphere 76 (2009) 907–914, https://doi.org/10.1016/j.chemosphere.2009.05.002.

[2] C.E. Smit, C. Posthuma-Doodeman, P.L.A. van Vlaardingen, F.M.W. de Jong, Ecotoxicity of imidacloprid to aquatic organisms: derivation of water quality standards for peak and long-term exposure, Hum. Ecol. RISK Assess. 21 (2015) 1608–1630, https://doi.org/10.1080/10807039.2014.964071.

[3] E.P. Benton, J.F. Grant, R.J. Nichols, R.J. Webster, J.S. Schwartz, J.K. Bailey, Risk assessment of imidacloprid use in forest settings on the aquatic macroinvertebrate community, Environ. Toxicol. Chem. 36 (2017) 3108–3119, https://doi.org/10.1002/etc.3887.

[4] C.P. Athanasekou, V. Likodimos, P. Falaras, Recent developments of TiO_2 photocatalysis involving advanced oxidation and reduction reactions in water, J. Environ. Chem. Eng. 6 (2018) 7386–7394, https://doi.org/10.1016/j.jece.2018.07.026.

[5] W.H.M. Abdelraheem, M.N. Nadagouda, D.D. Dionysiou, Solar light-assisted remediation of domestic wastewater by NB-TiO_2 nanoparticles for potable reuse, Appl. Catal. B Environ. 269 (2020), 118807, https://doi.org/10.1016/j.apcatb.2020.118807.

[6] M.M. Mahlambi, C.J. Ngila, B.B. Mamba, Recent developments in environmental photocatalytic degradation of organic pollutants: the case of titanium dioxide nanoparticles—a review, J. Nanomater. 2015 (2015) 1–29, https://doi.org/10.1155/2015/790173.

[7] X. Hu, X. Hu, C. Tang, S. Wen, X. Wu, J. Long, X. Yang, H. Wang, L. Zhou, Mechanisms underlying degradation pathways of microcystin-LR with doped TiO_2 photocatalysis, Chem. Eng. J. 330 (2017) 355–371, https://doi.org/10.1016/j.cej.2017.07.161.

[8] S. Escobedo, H. de Lasa, Photocatalysis for air treatment processes: current technologies and future applications for the removal of organic pollutants and viruses, Catalysts 10 (2020) 966, https://doi.org/10.3390/catal10090966.

[9] V. Etacheri, C. Di Valentin, J. Schneider, D. Bahnemann, S.C. Pillai, Visible-light activation of TiO_2 photocatalysts: advances in theory and experiments, J. Photochem. Photobiol. C Photochem. Rev. 25 (2015) 1–29, https://doi.org/10.1016/j.jphotochemrev.2015.08.003.

[10] X.H. Lin, Y. Miao, S.F.Y. Li, Location of photocatalytic oxidation processes on anatase titanium dioxide, Catal. Sci. Technol 7 (2017) 441–451, https://doi.org/10.1039/c6cy02214f.

[11] M. Rahbar, M. Mehrzad, M. Behpour, S. Mohammadi-Aghdam, M. Ashrafi, S, N co-doped carbon quantum dots/TiO_2 nanocomposite as highly efficient visible light photocatalyst, Nanotechnology 30 (2019), 505702, https://doi.org/10.1088/1361-6528/ab40dc.

[12] A. Datcu, M.L. Mendoza, A.P. del Pino, C. Logofatu, C. Luculescu, E. György, UV–vis light induced photocatalytic activity of TiO_2/graphene oxide nanocomposite coatings, Catal. Today 321–322 (2019) 81–86, https://doi.org/10.1016/j.cattod.2018.02.026.

[13] M. Nasr, C. Eid, R. Habchi, P. Miele, M. Bechelany, Recent progress on titanium dioxide nanomaterials for photocatalytic applications, ChemSusChem 11 (2018) 3023–3047, https://doi.org/10.1002/cssc.201800874.

[14] Z. Li, H. Bian, X. Xiao, J. Shen, C. Zhao, J. Lu, Y.Y. Li, Defective black TiO_2 nanotube arrays for enhanced photocatalytic and photoelectrochemical applications, ACS Appl. Nano Mater. 2 (2019) 7372–7378, https://doi.org/10.1021/acsanm.9b01878.

[15] L. Andronic, A. Enesca, Black TiO_2 synthesis by chemical reduction methods for photocatalysis applications, Front. Chem. 8 (2020), 565489, https://doi.org/10.3389/fchem.2020.565489.

[16] C. Belver, J. Bedia, M. Peñas-Garzón, V. Muelas-Ramos, A. Gómez-Avilés, J. J. Rodriguez, O. Sacco, V.B.T.-V.L.A.S.P. for the R. of E.C. Vaiano, Structured photocatalysts for the removal of emerging contaminants under visible or solar light, eds.. Visible Light Active Structured Photocatalysts for the Removal of Emerging Contaminants, Elsevier, 2020, pp. 41–98, https://doi.org/10.1016/B978-0-12-818334-2.00003-1.

[17] Z. Xiu, M. Guo, T. Zhao, K. Pan, Z. Xing, Z. Li, W. Zhou, Recent advances in Ti^{3+} self-doped nanostructured TiO_2 visible light photocatalysts for environmental and energy applications, Chem. Eng. J. 382 (2020), 123011, https://doi.org/10.1016/j.cej.2019.123011.

[18] A. Sarkar, G.G. Khan, The formation and detection techniques of oxygen vacancies in titanium oxide-based nanostructures, Nanoscale 11 (2019) 3414–3444, https://doi.org/10.1039/c8nr09666j.

[19] C. Di Valentin, G. Pacchioni, A. Selloni, Reduced and n-type doped TiO_2: nature of Ti^{3+} species, J. Phys. Chem. C (2009), https://doi.org/10.1021/jp9061797.

[20] S.G. Ullattil, S.B. Narendranath, S.C. Pillai, P. Periyat, Black TiO_2 nanomaterials: a review of recent advances, Chem. Eng. J. 343 (2018) 708–736, https://doi.org/10.1016/j.cej.2018.01.069.

[21] J. Li, M. Zhang, Z. Guan, Q. Li, C. He, J. Yang, Synergistic effect of surface and bulk single-electron-trapped oxygen vacancy of TiO_2 in the photocatalytic reduction of CO_2, Appl. Catal. B Environ. 206 (2017) 300–307, https://doi.org/10.1016/j.apcatb.2017.01.025.

[22] N.A. Deskins, R. Rousseau, M. Dupuis, Distribution of Ti^{3+} surface sites in reduced TiO_2, J. Phys. Chem. C 115 (2011) 7562–7572, https://doi.org/10.1021/jp2001139.

[23] A. Ziylan-Yavaş, N.H. Ince, Enhanced photo-degradation of paracetamol on n-platinum-loaded TiO_2: the effect of ultrasound and [rad]OH/hole scavengers, Chemosphere 162 (2016) 324–332, https://doi.org/10.1016/j.chemosphere.2016.07.090.

[24] E.M. Rodríguez, G. Márquez, M. Tena, P.M. Álvarez, F.J. Beltrán, Determination of main species involved in the first steps of TiO_2 photocatalytic degradation of organics with the use of scavengers: the case of ofloxacin, Appl. Catal. B Environ. 178 (2015) 44–53, https://doi.org/10.1016/j.apcatb.2014.11.002.

[25] L. Andronic, L. Isac, S. Miralles-Cuevas, M. Visa, I. Oller, A. Duta, S. Malato, Pilot-plant evaluation of TiO_2 and TiO_2-based hybrid photocatalysts for solar treatment of polluted water, J. Hazard. Mater. (2016), https://doi.org/10.1016/j.jhazmat.2016.08.013.

[26] L. Andronic, A. Enesca, C. Cazan, M. Visa, TiO_2–active carbon composites for wastewater photocatalysis, J. Sol Gel Sci. Technol. 71 (2014) 396–405, https://doi.org/10.1007/s10971-014-3393-6.

[27] L. Andronic, A. Vladescu, A. Enesca, Synthesis, characterisation, photocatalytic activity, and aquatic toxicity evaluation of TiO_2 nanoparticles, Nanomaterials 11 (2021) 3197, https://doi.org/10.3390/nano11123197.

[28] L. Andronic, L. Isac, C. Cazan, A. Enesca, Simultaneous adsorption and photocatalysis processes based on ternary TiO_2–CuxS–fly ash hetero-structures, Appl. Sci. 10 (2020) 8070, https://doi.org/10.3390/app10228070.

[29] H. Elbushra, M. Ahmed, H. Wardi, N. Eassa, Synthesis and characterization of TiO_2 using sol-gel method at different annealing temperatures, MRS Adv. 3 (2018) 2527–2535, https://doi.org/10.1557/adv.2018.230.

[30] NIST X-ray Photoelectron Spectroscopy Database, NIST Standard Reference Database Number 20, National Institute of Standards and Technology, Gaithersburg MD, 20899, 2000, https://doi.org/10.18434/T4T88K.

[31] H.R. An, S.Y. Park, H. Kim, C.Y. Lee, S. Choi, S.C. Lee, S. Seo, E.C. Park, Y.K. Oh, C. G. Song, J. Won, Y.J. Kim, J. Lee, H.U. Lee, Y.C. Lee, Advanced nanoporous TiO_2 photocatalysts by hydrogen plasma for efficient solar-light photocatalytic application, Sci. Rep. 6 (2016) 29683, https://doi.org/10.1038/srep29683.

[32] F. Liu, X. Yan, X. Chen, L. Tian, Q. Xia, X. Chen, Mesoporous TiO_2 nanoparticles terminated with carbonate-like groups: amorphous/crystalline structure and visible-light photocatalytic activity, Catal. Today 264 (2016) 243–249, https://doi.org/10.1016/j.cattod.2015.07.012.

[33] H. Liu, S. Liu, Z. Zhang, X. Dong, T. Liu, Hydrothermal etching fabrication of TiO_2@graphene hollow structures: mutually independent exposed {001} and {101} facets nanocrystals and its synergistic photocaltalytic effects, Sci. Rep. 6 (2016) 33839, https://doi.org/10.1038/srep33839.

[34] P. Krishnan, M. Liu, P.A. Itty, Z. Liu, V. Rheinheimer, M.-.H. Zhang, P.J. M. Monteiro, L.E. Yu, Characterization of photocatalytic TiO_2 powder under varied environments using near ambient pressure X-ray photoelectron spectroscopy, Sci. Rep. 7 (2017) 43298, https://doi.org/10.1038/srep43298.

[35] M. Thommes, K. Kaneko, A.V. Neimark, J.P. Olivier, F. Rodriguez-Reinoso, J. Rouquerol, K.S.W. Sing, Physisorption of gases, with special reference to the evaluation of surface area and pore size distribution (IUPAC Technical Report), Pure Appl. Chem. 87 (2015) 1051–1069, https://doi.org/10.1515/pac-2014-1117.

[36] F.J. Sotomayor, K.A. Cychosz, M. Thommes, Characterization of micro/mesoporous materials by physisorption: concepts and case studies, Acc. Mater. Surf. Res. 3 (2018) 34–50.

[37] W. Hu, W. Zhou, K. Zhang, X. Zhang, L. Wang, B. Jiang, G. Tian, D. Zhao, H. Fu, Facile strategy for controllable synthesis of stable mesoporous black TiO_2 hollow spheres with efficient solar-driven photocatalytic hydrogen evolution, J. Mater. Chem. A 4 (2016) 7495–7502, https://doi.org/10.1039/C6TA01928E.

[38] O.A. Journal, Detection of imidacloprid and bisphenol-S by solid phase extraction (SPE) coupled with UV-VIS spectrometer and LC-MS, Biointerface Res. Appl. Chem. 9 (2019) 4433–4438, https://doi.org/10.33263/BRIAC95.433438.

[39] W. Bahnemann, M. Muneer, M.M. Haque, Titanium dioxide-mediated photocatalysed degradation of few selected organic pollutants in aqueous suspensions, Catal. Today 124 (2007) 133–148, https://doi.org/10.1016/j.cattod.2007.03.031.

[40] J. Wang, A.S. Cherevan, C. Hannecart, S. Naghdi, S.P. Nandan, T. Gupta, D. Eder, Ti-based MOFs: new insights on the impact of ligand composition and hole scavengers on stability, charge separation and photocatalytic hydrogen evolution, Appl. Catal. B Environ. 283 (2021), 119626, https://doi.org/10.1016/j.apcatb.2020.119626.

[41] J.T. Schneider, D.S. Firak, R.R. Ribeiro, P. Peralta-Zamora, Use of scavenger agents in heterogeneous photocatalysis: truths, half-truths, and misinterpretations, Phys. Chem. Chem. Phys. 22 (2020) 15723–15733, https://doi.org/10.1039/d0cp02411b.

[42] K. Wetchakun, N. Wetchakun, S. Sakulsermsuk, An overview of solar/visible light-driven heterogeneous photocatalysis for water purification: TiO_2- and ZnO-based photocatalysts used in suspension photoreactors, J. Ind. Eng. Chem. 71 (2019) 19–49, https://doi.org/10.1016/j.jiec.2018.11.025.

[43] Y. Vasseghian, M. Berkani, F. Almomani, E.N. Dragoi, Data mining for pesticide decontamination using heterogeneous photocatalytic processes, Chemosphere 270 (2021), 129449, https://doi.org/10.1016/j.chemosphere.2020.129449.

[44] H. Song, C. Li, Z. Lou, Z. Ye, L. Zhu, Effective formation of oxygen vacancies in black TiO_2 nanostructures with efficient solar-driven water splitting, ACS Sustain. Chem. Eng. 5 (2017) 8982–8987, https://doi.org/10.1021/acssuschemeng.7b01774.

[45] R. Nawaz, C.F. Kait, H.Y. Chia, M.H. Isa, L.W. Huei, N.T. Sahrin, Synthesis of black-TiO_2 and manganese-doped TiO_2 nanoparticles and their comparative performance

evaluation for photocatalytic removal of phenolic compounds from agro-industrial effluent, J. Nanoparticle Res. 23 (2021) 263, https://doi.org/10.1007/s11051-021-05373-4.

[46] S. Wu, X. Li, Y. Tian, Y. Lin, Y.H. Hu, Excellent photocatalytic degradation of tetracycline over black anatase-TiO_2 under visible light, Chem. Eng. J. 406 (2021), 126747, https://doi.org/10.1016/j.cej.2020.126747.

[47] R. Katal, M. Salehi, M.H. Davood Abadi Farahani, S. Masudy-Panah, S.L. Ong, J. Hu, Preparation of a new type of black TiO_2 under a vacuum atmosphere for sunlight photocatalysis, ACS Appl. Mater. Interfaces 10 (2018) 35316–35326, https://doi.org/10.1021/acsami.8b14680.

[48] Z. Yan, W. Huang, X. Jiang, J. Gao, Y. Hu, H. Zhang, Q. Shi, Hollow structured black TiO_2 with thickness-controllable microporous shells for enhanced visible-light-driven photocatalysis, Microporous Mesoporous Mater. 323 (2021), 111228, https://doi.org/10.1016/j.micromeso.2021.111228.

[49] Z. Miao, G. Wang, L. Li, C. Wang, X. Zhang, Fabrication of black TiO_2/TiO_2 homojunction for enhanced photocatalytic degradation, J. Mater. Sci. 54 (2019) 14320–14329, https://doi.org/10.1007/s10853-019-03900-2.

[50] J. Xi, Y. Zhang, X. Chen, Y. Hu, A simple sol–gel hydrothermal method for the synthesis of defective TiO_2 nanocrystals with excellent visible-light photocatalytic activity, Res. Chem. Intermed. 46 (2020) 2205–2214, https://doi.org/10.1007/s11164-020-04087-x.

[51] S. Saensook, A. Sirisuk, A factorial experimental design approach to obtain defect-rich black TiO_2 for photocatalytic dye degradation, J. Water Process Eng. 45 (2022), 102495, https://doi.org/10.1016/j.jwpe.2021.102495.

[52] J. Li, E.H. Wu, J. Hou, P. Huang, Z. Xu, Y. Jiang, Q.S. Liu, Y.Q. Zhong, A facile method for the preparation of black TiO_2 by Al reduction of TiO_2 and their visible light photocatalytic activity, RSC Adv. 10 (2020) 34775–34780, https://doi.org/10.1039/d0ra06784a.

[53] Y. Ding, Y. Wu, T. Zhang, L. Tao, X. Liu, X. Liu, L. Hu, T. Hayat, A. Alsaedi, S. Dai, Colorful TiO_{2-x} microspheres cooperating with titanium Schiff base complex for efficient visible light photocatalysts, Catal. Today 335 (2019) 550–556, https://doi.org/10.1016/j.cattod.2019.03.004.

[54] M. Ji, Y.H. Choa, Y.I. Lee, One-step synthesis of black TiO_{2-x} microspheres by ultrasonic spray pyrolysis process and their visible-light-driven photocatalytic activities, Ultrason. Sonochem. 74 (2021), 105557, https://doi.org/10.1016/j.ultsonch.2021.105557.

[55] U.I. Gaya, A.H. Abdullah, Heterogeneous photocatalytic degradation of organic contaminants over titanium dioxide: a review of fundamentals, progress and problems, J. Photochem. Photobiol. C Photochem. Rev. 9 (2008) 1–12, https://doi.org/10.1016/j.jphotochemrev.2007.12.003.

[56] Z. Bielan, S. Dudziak, A. Sulowska, D. Pelczarski, J. Ryl, A. Zielińska-Jurek, Preparation and characterization of defective TiO_2. The effect of the reaction environment on titanium vacancies formation, Materials 13 (2020) 1–25, https://doi.org/10.3390/ma13122763. Basel.